 doi:10.20944/preprints202203.0406.v1

Article

Aerosol optical thickness retrieval in presence of cloud: application to S3A/SLSTR observations.

Marta Luffarelli [1,*], Yves Govaerts [1] and Lucio Franceschini [1,]

[1] Rayference, 1030, Brussels, Belgium
* Correspondence: marta.luffarelli@rayference.eu

Abstract: The Combined Inversion of Surface and AeRosols (CISAR) algorithm for the joint retrieval of surface and aerosol single scattering properties has been further developed in order to extend the retrieval to clouds and overcome the need for an external cloud mask. Pixels located in the transition zone between pure cloud and pure aerosol are often discarded by both aerosol and cloud algorithms, despite being essential for studying aerosol-cloud interactions, which still represent the largest source of uncertainty in climate predictions. The proposed approach aims at filling this gap and deepening the understanding of aerosol properties in cloudy environments. The new CISAR version is applied to Sentinel-3A/SLSTR observations and evaluated against different satellite products and ground measurements. The spatial coverage is greatly improved with respect to algorithms processing only pixels flagged as clear sky by the SLSTR cloud mask. The continuous retrieval of aerosol properties without any safety zone around clouds opens new possibilities for studying aerosol properties in cloudy environments.

Keywords: aerosols; clouds; inversion; optimal estimation

1. Introduction

Aerosol particles play a fundamental role in the Earth's climate by reflecting and absorbing the incoming solar radiation. Anthropogenic aerosols have been identified as one of the main contributors to climate forcing, and their interactions with clouds continue to contribute the largest uncertainty to the total radiative forcing (RF) estimate [1]. Aerosols, or more precisely fine mode (FM) aerosol particles, can act as cloud condensation nuclei (CCN), altering cloud properties and their radiative effects. Moreover, aerosols have an impact on human health, with ambient air pollution causing over 4 million premature deaths yearly [2]. Dust events such as, for instance, sand storms coming from the Sahara region, affect not only the climate and human health, but also affect the correct functioning of solar panels installation. Given the above considerations, it is clear that observing and understanding aerosol properties is a crucial point for the remote sensing community.

Normally, aerosol retrieval from satellite remote sensing relies on a preliminary cloud masking algorithm to separate cloudy and clear sky observations; the retrieval is thus performed only on clear-sky pixels. An experiment performed in the framework of the European Space Agency (ESA) aerosol climate change initiative (CCI) project showed how applying different cloud masks to the same aerosol retrieval algorithm can strongly impact the algorithm performances [3]. Cloud detection algorithms are usually based on physical principles, but threshold values used to identify cloudy and cloud-free pixels can vary according to the application. An accurate cloud masking can strongly improve the aerosol retrieval as it reduces the possibility of cloud contamination, which probability increases at coarser resolutions [4], and the adjacency effect, which could lead to an enhancement of the measured top-of-atmosphere (TOA) bidirectional reflectance factor (BRF) and in turn to an overestimated aerosol optical thickness (AOT). Because of the TOA BRF enhancement due to adjacent clouds, the aerosol retrieval is strongly dependent on the quality of the cloud mask used to classify cloud-free pixels [3].

To minimise the effect of the TOA BRF enhancement and thus the overestimation of low AOT, the cloud mask in aerosol retrieval applications normally takes into account

 doi:10.20944/preprints202203.0406.v1

a safety zone around cloud particles [5]. For instance, in the above-mentioned Aerosol-CCI experiment, this safety zone had an extent of 10 km. However, even after such a conservative cloud masking, it is shown that the retrieved AOT tends to be higher in the vicinity of clouds ([6], [7]). Analysing MODIS data, [8] found that the retrieved AOT was 25% larger with cloud fraction (CF) of 0.8-0.9 than in relatively cloud-free conditions (CF=0.1-0.2). Moreover, due to such a conservative cloud mask, a large amount of pixels are "lost", discarded by both aerosol and cloud algorithms. [9] calculated that in the case of MODIS 20% of all pixels are discarded by both aerosol and cloud algorithms. Given the primary role of aerosol-cloud interactions (ACI) in the uncertainty estimation of radiative forcing by climate change models, the transition zone between clear and cloudy sky is currently receiving increasing attention ([10], [11], [12]). Aerosol particles near clouds become more hydrating and swell in size, resulting in increased AOT [13]. Clouds are also sources of aerosols, generating new particles through aqueous chemistry and subsequent evaporation; these particles may have very different optical properties than those particles initially available [14]. Given the above considerations, this transition zone and the changes in aerosol properties in the vicinity of clouds is not necessarily an artefact and should be studied extensively ([15], [16]). Since AOT is normally retrieved only in cloud-free conditions, the total AOT measured from satellites is most likely underestimated, with a subsequent underestimation of the aerosol direct radiative effect [17]. On the other hand, processing pixels in the vicinity of clouds could lead to a significant overestimation of the AOT, as any enhancement of the TOA BRF in these pixels would be attributed to aerosols. It should be noted here, however, that in inversion algorithms based on 1D radiative transfer models (RTMs), any 3D effects between clouds and clear-sky pixels cannot be correctly characterised.

The new version of the Combined Inversion of Surface and AeRosols (CISAR) algorithm ([18], [19]) presented in this paper addresses some of the issues related to clouds in the aerosols retrieval. After a short training period, the new algorithm no longer relies on an external cloud mask, meaning that cloudy observations and pixels located in the safety zone between clear and cloudy sky will be processed with the same radiative assumptions as cloud-free pixels. Such a product could improve our understanding of aerosol properties in the vicinity of clouds. Also, high aerosol events are often misclassified as clouds from several cloud masking algorithms; without relying on an external cloud mask CISAR is capable of retrieving such events. Section 2 describes the data used for this study and the new features of the CISAR algorithm with respect to [18], which allow CISAR to address the new challenges introduced by the processing of cloudy pixels. A case study over a dust storm originating from Sahara and moving towards the Caribbean islands will be presented in Section 3, where CISAR retrieval will be evaluated against cross satellite products and ground observations.

2. Data and method

2.1. The SLSTR instrument

The Sea and Land Surface Temperature Radiometer (SLSTR) instrument, designed to maintain continuity with the (A)ATSR series of instruments, is one of the instruments onboard Sentinel-3, an Earth constellation developed by ESA in the framework of the Copernicus programme. Despite being primarily an ocean mission, Sentinel-3 is proven suitable for atmospheric and land applications. The constellation consists of two satellites: Sentinel-3A, launched on February 16, 2016, and Sentinel-3B, launched on April 25, 2018. The Sentinel-3 satellites are polar-orbiting, flying at an altitude of 815 km with a local equatorial crossing time of 10:00 am. SLSTR covers 9 spectral bands located between 0.55 μm and 12 μm, of which only the 6 reflective bands (S1 to S6) are considered in this study. Of particular interest is the band S4, centred at 1.37 μm on a pick of water vapour absorption. This band is used for cirrus detection over land. One of the interesting features of the instrument in the framework of atmospheric application is the dual view. Images are acquired at nadir and at an angle of 55°, with swath widths equal to 1420 km and 750

Preprints (www.preprints.org) | NOT PEER-REVIEWED | Posted: 31 March 2022 doi:10.20944/preprints202203.0406.v1

km respectively. The dual view of the SLSTR instrument allows a revisit time of 1.9 days at the equator and 1.5 days at latitudes higher than 30°. However, the oblique view is in opposite direction compared to (A)ATSR, hence in the backscattering direction in the northern hemisphere [20]. The impact of this geometric configuration on the information content associated with the satellite observation is analysed in Section 2.3.1. This study is based on SLSTR on-board Sentinel-3A acquisitions, aggregated at 10 km super-pixels. The aggregation still exploits the summary cloud mask in the SLSTR Level-1 product as follows:

- if the 80% of sub-pixels are cloud-free only cloud-free observations are aggregated and the cloud mask is set to 0.
- if the 80% of sub-pixels are cloudy only cloudy observations are aggregated and the cloud mask is set to 1.
- Otherwise, all pixels are aggregated and the cloud mask is a number between 0 and 1 indicating the percentage of cloudy pixels.

2.2. The CISAR algorithm

The CISAR algorithm has been developed to address the limitations of a Look-Up-Table (LUT) based approach and the consistency issues that arise from retrieving different Earth system components with dedicated algorithms. CISAR is based on the online inversion of a fast RTM, which allows the retrieval of surface reflectance and aerosol single scattering properties (optical thickness, single scattering albedo and asymmetry factor), with continuous variation of the state variable in the solution space [18]. The inversion is performed with an optimal estimation (OE) approach, a strict mathematical framework that seeks the best balance between the information coming from the observation and any prior information on the observed system. Satellite observations are accumulated during the so-called accumulation period, the length of which varies according to the satellite characteristics. During the accumulation period, the surface reflectance properties are considered constant, while the aerosol and cloud single scattering properties are retrieved at each satellite acquisition.

The algorithm is applicable to any sensor acquiring observations in the visible spectral region, and its performances, when applied to radiometers flying at different orbits (polar-orbiting and geostationary), have been analysed in [19]. As other aerosol retrieval algorithms ([21], [22]), CISAR tends to overestimate low AOTs. Identifying the cloud effects as one of the causes of this overestimation and given the strong dependency of aerosol retrieval on the cloud masking [3], CISAR has been extended to the retrieval of cloud single scattering properties, overcoming the need of an external cloud mask. This innovative approach aims at improving the spatial coverage of aerosol products, reducing the amount of "lost pixels" discarded by both aerosol and cloud retrieval algorithms. By extending the retrieval to the vicinity of clouds, the CISAR algorithm paves the way for a deeper understanding of aerosol properties in cloudy environments.

2.2.1. CISAR atmospheric solution space

The CISAR aerosol properties solution space is defined as the portion of the 2-dimensional single scattering albedo (ω) and asymmetry factor (g) space delimited by three selected aerosol vertices. The latter represent absorbing and non-absorbing fine mode and coarse mode particles [18]. The inversion process retrieves the AOT associated with each vertex. The asymmetry factor and the single scattering albedo are then calculated as a mean of the properties associated with the three vertices weighted by the retrieved optical thickness:

$$\begin{aligned} \omega_{T_A} &= \frac{\tau_{FN}\omega_{FN} + \tau_{FA}\omega_{FA} + \tau_C\omega_C}{\tau_{FN} + \tau_{FA} + \tau_C} \\ g_{T_A} &= \frac{\tau_{FN}g_{FN} + \tau_{FA}g_{FA} + \tau_C g_C}{\tau_{FN} + \tau_{FA} + \tau_C} \end{aligned} \quad (1)$$

Preprints (www.preprints.org) | NOT PEER-REVIEWED | Posted: 31 March 2022 doi:10.20944/preprints202203.0406.v1

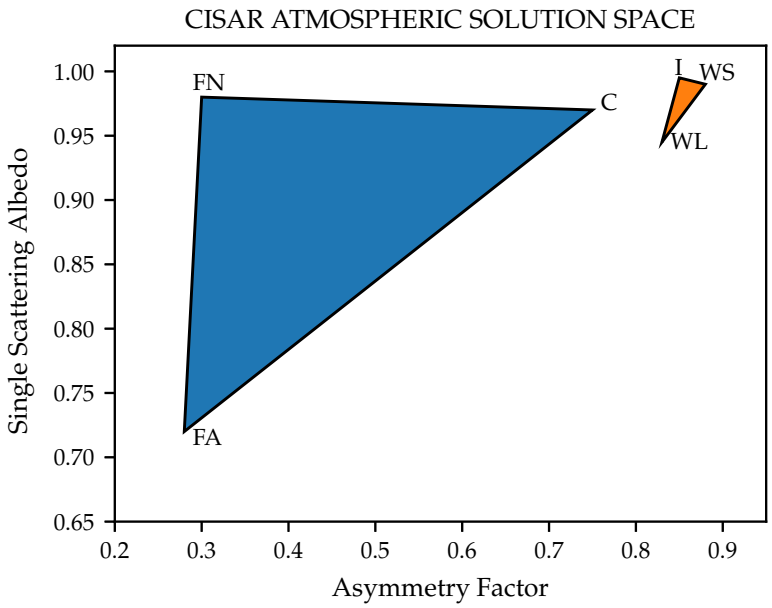

Figure 1. Example of the CISAR solution space for aerosol and cloud single scattering properties. the x-axis represents the asymmetry factor and the y axis represents the single scattering albedo. The blue triangle represents the solution space for the aerosol particles, delimited by the three vertices associated with fine absorbing (FA), fine non-absorbing (FN) and coarse (C) mode particles. The orange triangle is the solution space in which the cloud properties are allowed to change, delimited by the vertices representing small and large water (WS and WL respectively) and ice (I) particles.

To extend the retrieval to cloud single scattering properties, three cloud vertices are defined to sample a different portion of the ω-g space (Fig. 1). The selected vertices represent small and large liquid and ice particles. The cloud single scattering properties are calculated similarly as in Eq. 2:

$$\begin{aligned} \omega_{T_C} &= \frac{\tau_{WL}\omega_{WL} + \tau_{WS}\omega_{WS} + \tau_I\omega_I}{\tau_{WL} + \tau_{WS} + \tau_I} \\ g_{T_C} &= \frac{\tau_{WL}g_{WL} + \tau_{WS}g_{WS} + \tau_I g_I}{\tau_{WL} + \tau_{WS} + \tau_I} \end{aligned} \tag{2}$$

Nevertheless, the forward model used within CISAR, FASTRE, only has one scattering layer: this prevents the determination of the position of the aerosol layer with respect to the clouds. It is stressed here that the retrieval of cloud single scattering properties is considered a bypass product, and the main focus of the CISAR algorithm remains the retrieval of aerosol particles.

2.2.2. Prior information

Within CISAR, the inversion is performed in an OE framework, which seeks the best balance between the information coming from the observation and the prior information, which consists of any additional knowledge on the observed scene. Constraints are applied to the surface reflectance and AOT magnitude, as well as to the temporal and spectral variability of the state variables. The latter is now applied to the cloud single scattering properties as well, helping the discrimination between aerosols and clouds. The new version of the algorithm requires an additional source of prior information associated with the cloud optical thickness (COT). Besides the prior information already discussed in [19], new features are introduced for the prior information on the aerosol and cloud properties and on the surface reflectance.

Preprints (www.preprints.org) | NOT PEER-REVIEWED | Posted: 31 March 2022 doi:10.20944/preprints202203.0406.v1

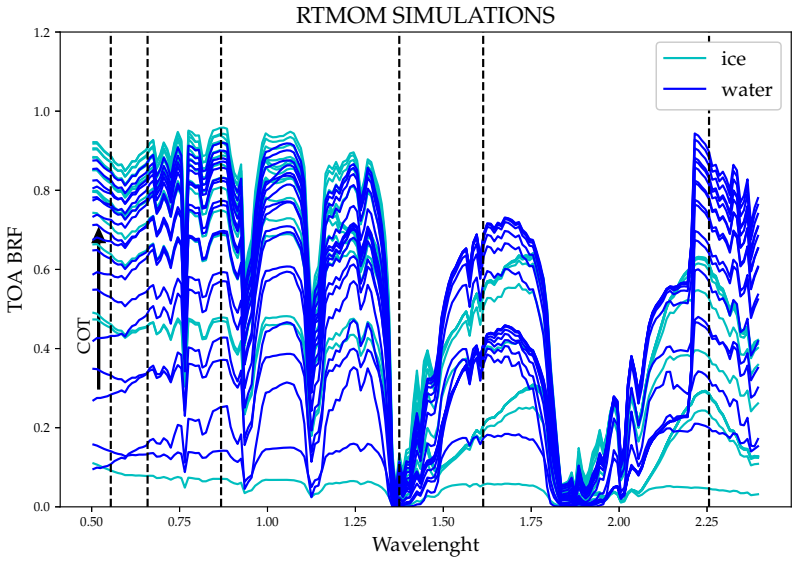

Figure 2. Results from the RTMOM simulations on ice (cyan) and liquid (blue) particle of different radius, with associated Cloud Optical Thickness (COT) varying from 1 to 80. The dashed vertical lines represent the S3A/SLSTR bands from S1 to S6.

Cloud phase and optical thickness

To develop meaningful prior information on the COT, the spectral signature of clouds has been simulated in the relevant part of the spectrum through the Radiation Transfer Matrix Operator Model (RTMOM, [23]), which accuracy has been extensively documented [24]. Simulations have been made considering a wide range of particle size, compositions and COT values. Figure 2 shows partial results of the RTMOM simulations for liquid (blue) and ice (cyan) clouds. The TOA BRF magnitude increases with the COT, although it tends to saturate for high values of COT. These results suggest that it is possible to build suitable prior information analysing the spectral behaviour of clouds in the spectral bands of the radiometer being processed. When applied to SLSTR data, the prior information on the cloud optical thickness is built considering the ratio between the TOA BRF in band S1 and the one in band S4. Figure 3 shows the values that this ratio takes for the above mentioned RTMOM simulations. Given the evolution of the curves in Figure 3a the prior information on the cloud COT is built as in Eq. 3:

$$\hat{x}_{\tau_{cloud}} = 1.4 \times \exp\left(35. \times \frac{y_{0S4}}{y_{0S1}}\right), \tag{3}$$

where $\hat{x}_{\tau_{cloud}}$ is the magnitude of the prior on the total COT and $y_{0S1,S4}$ the TOA BRF in SLSTR bands S1 and S4 respectively.

The cloud phase discrimination can thus be built considering the ratio between the TOA BRF in bands S6 and S1: ice clouds are brighter at shorter wavelengths and darker in band S6, whereas liquid water clouds show opposite behaviour (3b).

Spatial constraints on AOT

One of the main technical advantages of the CISAR algorithm implementation is the ability to perform the inversion at the pixel-level, meaning that the inversion of a pixel is fully independent. This allows a full parallelisation of the code at a core level, as each pixel can be processed on a dedicated core independently from any surrounding pixel. While preserving this feature, spatial smoothing has been implemented, as aerosols are supposed to have a slow spatial variability in a few tenths of kilometres of the spatial

Preprints (www.preprints.org) | NOT PEER-REVIEWED | Posted: 31 March 2022 doi:10.20944/preprints202203.0406.v1

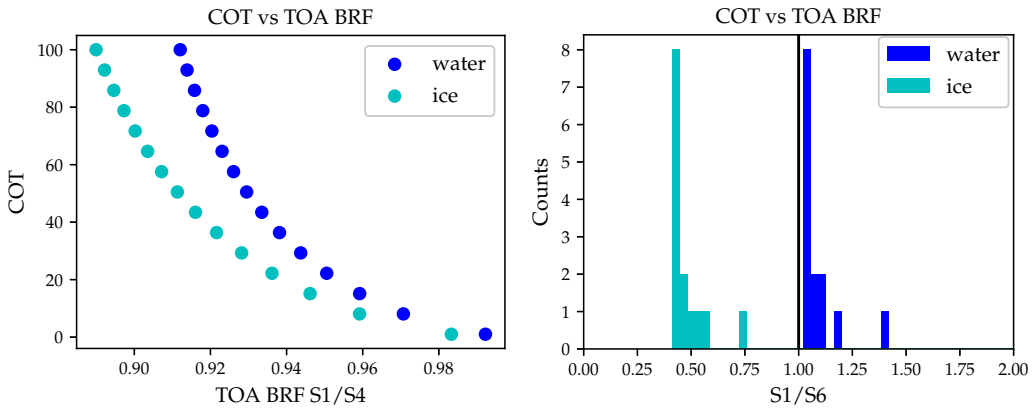

(a) **(b)**

Figure 3. The left panel shows the plot of the simulated COT values (y axis) with respect to the ratio between the Top-Of-Atmosphere (TOA) Bidirectional Reflectance Factor (BRF) in band S1 and S4 (x axis) for both ice (cyan) and liquid (blue) clouds. The right panel shows the histogram of the distribution of the ratio between the TOA BRF in bands S1 and S6. The color code follows from Figure 2. It can been seen that the ratio is always larger than one (S1 brighter than S6) for ice clouds, while the opposite is true for water clouds.

window. This is achieved by exploiting the temporal overlap between two successive accumulation periods (see Sec. 2.2) and using the solution retrieved in the first period to build the prior information in the second. In particular, for each solution retrieved during the period P_i at pixel p a weighted mean is computed over the surrounding $N_p \times N_p$ pixels, accounting for the distance from the central pixel, and used as prior information for the same pixel at the period P_{i+1}. The value of N_p is chosen according to the spatial resolution. Within this study, N_P is set equal to 3, which corresponds to a 30x30 km window.

Surface parameters climatology

The retrieval of the surface reflectance is strongly complicated in cloudy conditions. The accurate retrieval of the surface reflectance is, however, necessary for the correct retrieval of atmospheric properties for a physically-based algorithm such as CISAR, taking into account the radiative coupling between the surface and the atmosphere. To maintain the ability to correctly retrieve the surface reflectance, and thus correctly account for the radiative coupling between surface and atmosphere, the CISAR prior information on the surface parameters has been improved by analysing the MODIS/MAIAC MCD19A3 product [26]. A new Rahman-Pinty-Verstraete (RPV, [27]) global climatology is prepared by averaging the MODIS RossThick/Li-Sparse (RTLS, [28]) parameters during 10 years (2010-2020) over the four seasons and converting them to RPV parameters in the SLSTR bands. The new climatology is used as default prior information on the RPV surface parameters at the very first accumulation period. For the successive accumulation periods, the prior is updated as explained in [19]. The new climatology is also analysed and used to define spectral constraints on the surface model parameters in the sensor bands. In the case of SLSTR, a strong spectral relation in the magnitude of the reflectance is found between bands S1-S2 and S5-S6. These spectral constraints are considered valid for any type of land cover, except for snow coverage, where the surface reflectance shows a very different spectral signature, with large values at shorter wavelengths (Figure 4). For this reason, snow pixels are currently disregarded by the processing. Snow coverage is identified by computing the normalised-difference snow index (NDSI) from bands S1 and S6 [29]. Pixels showing a NDSI larger than 0.75 are classified as snow and discarded by the processing. The implementation of the surface spectral constraints has a large positive impact on the

Preprints (www.preprints.org) | NOT PEER-REVIEWED | Posted: 31 March 2022 doi:10.20944/preprints202203.0406.v1

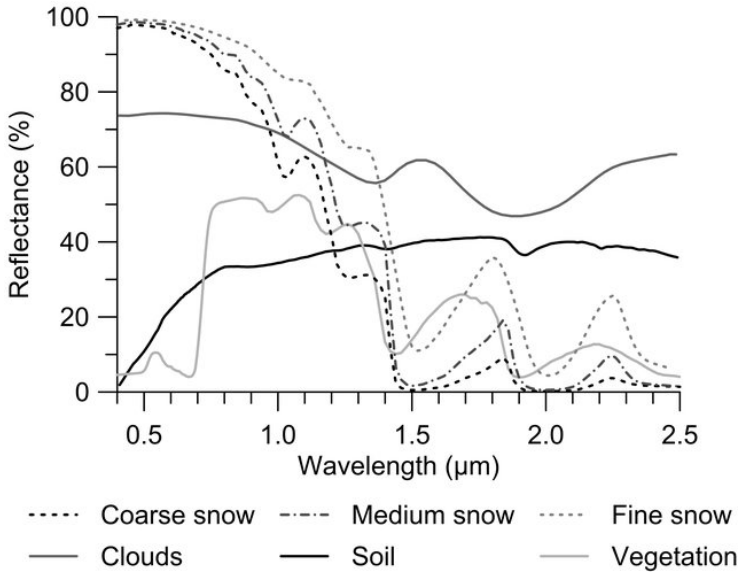

Figure 4. Representative spectral reflectance of snow, clouds, soil and vegetation in the visible and infrared range. After [25].

retrieval of the surface reflectance, as it improves the discrimination between cloud and surface contribution. A future version of the CISAR algorithm will include different spectral constraints to be activated in case of snow coverage.

2.3. Inversion

2.3.1. SLSTR data accumulation

S3A/SLSTR satellite images are accumulated during an accumulation period of 16 days (see Section 2.2), to build a multi-angular observation vector [19]. The accumulation periods are shifted by 12 days. The shift has been chosen in order to maximise the performances in terms of processing time while keeping an overlap between two consecutive periods where the spatial constraints discussed in Section 2.2.2 are applied. The availability of different acquisition geometries strongly impacts the information content of the observations [30]. The SLSTR dual view, however, introduces a clear difference between the Northern and Southern Hemispheres, as the oblique view is always observing in the backward scattering direction for latitude above about 20°South [31]. This particular feature is quantitatively analysed in Figure 5. The polar plot shows how Lindenberg, located in the Northern Hemisphere (Fig. 5a), is always observed in the backward scattering configuration, while this is not the case for Bandung, located in the Southern Hemisphere (Fig. 5b). The information content associated with aerosols is limited in the backward scattering direction, as aerosol particles mostly scatter in the forward direction, given the positive sign of the asymmetry factor g [32]. The time series in Figure 5 show that as the $cosg$ (cosine of the scattering angle) approaches zero and negative values, the Jacobian (i.e. the partial derivative of the TOA BRF with respect to the state variable) associated with the aerosol optical thickness decreases. In Figure 5 the large difference in the information content between the two hemispheres, quantified by the magnitude of the Jacobian, is visible. Given the above considerations, CISAR is expected to show better aerosol retrieval performances in the Southern Hemisphere.

Preprints (www.preprints.org) | NOT PEER-REVIEWED | Posted: 31 March 2022 doi:10.20944/preprints202203.0406.v1

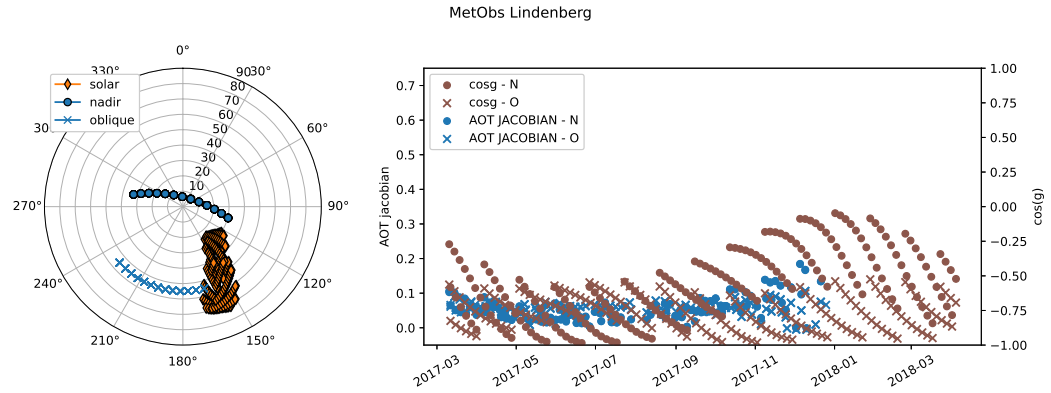

(a)

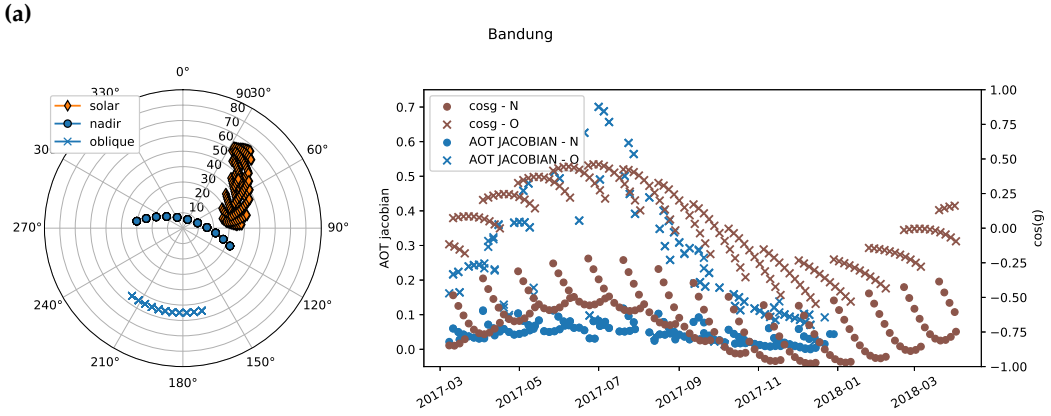

(b)

Figure 5. The polar plots (left panels) show the acquisition geometry over Lindenberg, Germany (52.209°N, 14.121°E) and Bandung, Australia (6.888°S, 107.610°E). The orange diamonds represent the solar angles, blue symbols represent the viewing angles. Circles represent the zenith angle and polar angles represent azimuth angles with zero azimuth pointing to the North. The right panels show the time series of the aerosol optical thickness (AOT) Jacobians (blue, left axis) and the cosine of the scattering angle (brown, right axis) from March 2017 to March 2018. Dots and crosses represent the nadir and oblique views respectively.

2.3.2. Data processing

Processing over land

The SLSTR observations accumulated as described in Sec. 2.3.1, together with all the necessary ancillary information (surface pressure, wind speed, total column water vapour, total column ozone, aerosol layer height) are inverted by the CISAR algorithm. The processing of cloudy observations implies new challenges with respect to algorithms retrieving only aerosol properties. One of the main issues associated with the processing of clouds with the CISAR algorithm is that the surface is not visible under thick clouds. Figure 6 shows the magnitude of the Jacobian associated with the four RPV parameters with respect to the retrieved COT. These results are obtained from the processing of one year of data over 16 AERONET stations with different locations and land cover. It can be seen that the Jacobians rapidly converge towards 0 as the COT increases. To address this issue, the CISAR algorithm is first trained with two cloud-free accumulation periods before discarding the use of the pre-processed cloud mask. In this way, the surface reflectance retrieved in the first two cloud-free accumulation periods is used to build strong prior information for the next periods, where no cloud mask is applied to classify the satellite observations. This so-called memory mechanism is explained in detail in [19]. However, it must be noted that mostly cloudy accumulation periods are still likely to happen. In order to not compromise the prior information on the surface with cloud contaminated information, the RPV parameters are set equal to the prior information when the average

Preprints (www.preprints.org) | NOT PEER-REVIEWED | Posted: 31 March 2022 doi:10.20944/preprints202203.0406.v1

retrieved COT within the accumulation period is larger than 5. In other words, no surface reflectance retrieval is taking place when the average COT during the whole accumulation period exceeds 5.

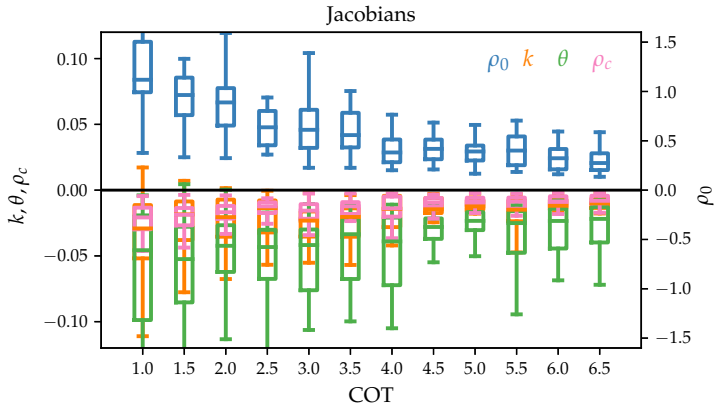

Figure 6. Magnitude of the Jacobian associated with each parameter of the Rahman-Pinty-Verstraete (RPV) surface model in function of the CISAR retrieved COT. Given the different order of magnitude among the Jacobians, two scales are here used to better visualise the Jacobian dependency on the COT. The right y-axis is related to the ρ_0, associated with the surface reflectance magnitude, the left y-axis is related to k, θ and ρ_c, associated with the surface reflectance shape.

Also, aerosol and cloud retrieval is particularly challenging over bright soil, where the signal from the surface is dominant [33]. However, both the aerosol and the cloud contributions are lower at 2.2 μm than in the lower part of the visible spectrum, whereas the surface reflectance of bright soil increases with the wavelength. CISAR exploits this feature by setting a very low prior on the magnitude of the COT (equal to 10^{-2}) when the TOA BRF in band S1 is larger than the one in band S6 and the retrieved ρ_0 surface parameter, which controls the magnitude of the surface reflectance, is larger than 0.2 in band S1.

Processing over water

Cloud masking over water is generally less problematic than over land and it is often based on thresholds at wavelengths in the NIR spectral region [34]. However, high aerosol events with larger particles, such as dust storms over the ocean, can be sometimes flagged as clouds by a threshold-based cloud masking algorithm. Within CISAR, three situations are defined based on the TOA BRF in band S6:

1. clear sky if TOA BRF in band S6 lower than 0.01;
2. cloudy if TOA BRF in band S6 larger than 0.2;
3. undefined otherwise;

If a pixel is flagged as cloud-free (cloudy), then prior on the COT (AOT) is set to 10^{-2} with equal uncertainty. If a pixel falls in the undefined case, the prior for the aerosol and cloud classes is prepared as in Section 2.2.2.
One exception to the above-mentioned cases is thick dust plumes over water. As dust and clouds have very similar spectral signatures, dust storms are often misclassified as clouds by many cloud masking algorithms [35]. However, dust and clouds show some differences in the visible bands (S1, S2 and S3 in the case of SLSTR) which make clouds appear as white and thick dust brown-ish in a false colour composite image (see Figure 7 and the Video S1 in the supplementary material) [36]. In particular, if $y_{0,S3} > 0.95 y_{0,S2}$ and $y_{0,S2} > 1.04 y_{0,S1}$ then a pixel is flagged as dust and the prior information on the AOT associated with the coarse mode is set to 2.5.

Preprints (www.preprints.org) | NOT PEER-REVIEWED | Posted: 31 March 2022 doi:10.20944/preprints202203.0406.v1

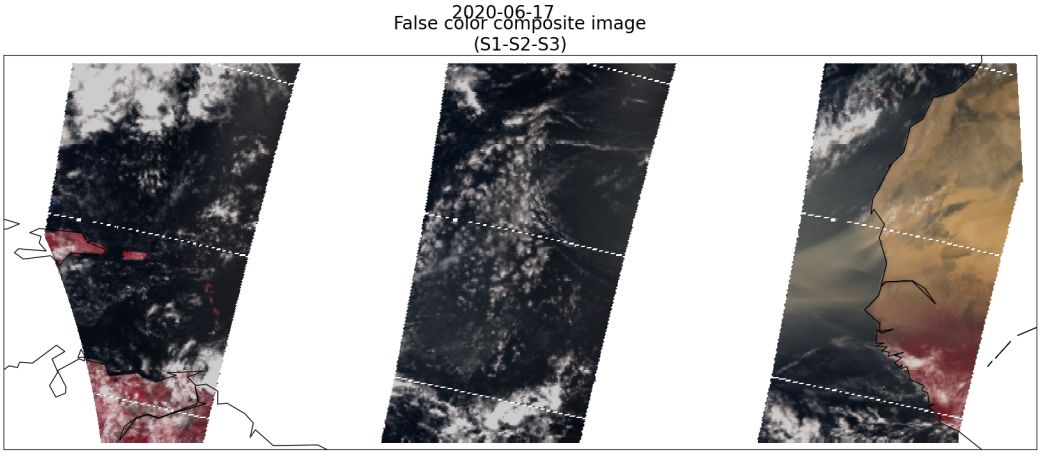

Figure 7. False color composite obtained from SLSTR bands S1, S2 and S3 over the Atlantic ocean during the 17th of June 2020. A thick dust plume is visible at the Western coast of Africa.

3. Case Study: The Godzilla dust storm

Sand and dust storms are extreme and rapidly evolving meteorological phenomena that generate significant amounts of mineral particles in the atmosphere. Desert dust represents a major portion of the global aerosol burden [37] and plays an important role in earth's radiative balance [38]. The Sahara desert is the world's first source of dust, accounting for 40-70% of the global amount of dust in the atmosphere [39]. Unfortunately, dust storms observed by satellite remote sensing are often misclassified as clouds, as the spectral signature of dust is very similar to the one of clouds [40].

Every year, Saharan dust is transported towards the Caribbean islands; this phenomenon reaches its maximum during summer months [41]. In particular, in June 2020 a dust plume originating from Sahara was transported towards the Caribbean islands, travelling more than 8000 km and peaking between the 14th and the 20th of June. This dust storm was so extreme that it has been named Godzilla. This extraordinary dust plume, nearly as big as the continental United States, weighed almost 24 million tons. Godzilla was surprising not only in terms of size and weight but also in terms of its trigger. Typically, the dust storms are driven by warm, moist air from monsoons on the southern edge of the Sahara that blows to the north; Godzilla, on the other hand, was triggered by a large patch of high-pressure air parked over the north-western edge of Africa [42]. Starting from the 14th of June, strong winds blowing at more than 70 km/h transported the dust storm lifting it up to 6 km into the atmosphere, which is higher than the 5 km for the climatological summertime extreme dust events [43]. The Godzilla dust storm was partially predicted by climate models such as the Copernicus Atmosphere Monitoring Service (CAMS) [44]. However, time series of the predicted AOT from CAMS reanalysis show some underestimation of high values of AOT with respect to AERONET.

Most of the dust storm is unfortunately misclassified as cloud from the SLSTR summary cloud flag (see Figure 8). Aerosol retrieval algorithms only inverting clear-sky observations, would therefore completely miss such an exceptional event. Conversely, the CISAR algorithm, not relying on an external cloud mask, performs the retrieval over all SLSTR observations regardless of the cloud mask classification. Figure 8 shows the false colour composite obtained from SLSTR bands S1, S2 and S3, the SLSTR summary cloud flag, the combined AOT and COT retrieval at 0.55 µm with the CISAR algorithm and the FM fraction associated to the AOT retrieval. It can be seen that most of the dust storm, partially visible in the false colour composite, is flagged as cloud. In particular, about 85% of SLSTR observations in Figure 8 are flagged as cloud; with a retrieval algorithm only inverting clear-sky observations, the aerosol retrieval would be performed only on the remaining 15% of the pixels. CISAR, however, retrieves valid AOT (*i.e.* greater than 0.) over 35% of all SLSTR observations, greatly improving the spatial coverage of the AOT

Preprints (www.preprints.org) | NOT PEER-REVIEWED | Posted: 31 March 2022 doi:10.20944/preprints202203.0406.v1

product. Finally, the thick dust plume visible in the false colour composite is correctly retrieved as coarse mode by CISAR, as seen in the bottom right panel in Figure 8 and in Video S2 in the supplementary material. From the animation, it can be seen that the thick Godzilla dust plume is retrieved as coarse mode (FM Fraction close to 0.), although the fine-coarse mode discrimination is less accurate as the dust plume becomes optically thinner (around the 20th of June). From the supplement material, it can also be observed an increase in the FM fraction close to clouds, similarly to what was observed by [45] analysing MODIS images and AERONET products. [45] found that the high AOT close to cloud edges exhibits high-frequency variability possibly resulting from the turbulent environment in the immediate vicinity of convective cells.

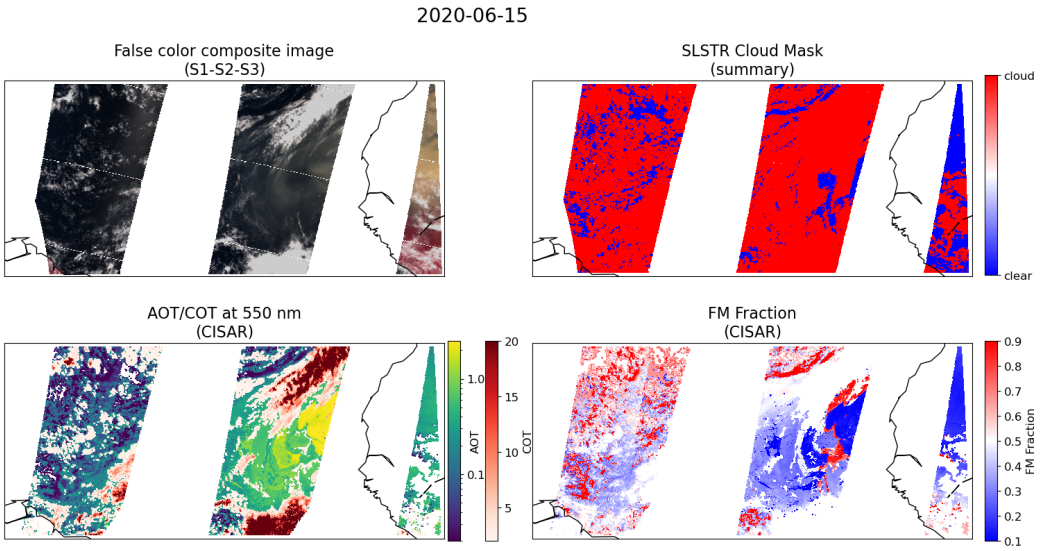

Figure 8. Top left panel: false color composite obtained from SLSTR bands S1, S2 and S3. Top right panel: SLSTR summary cloud mask, where blue indicates clear sky and red indicates cloud. Bottom left panel: combined AOT/COT retrieval at 0.55 µm with the CISAR algorithm. Only COT>2. is shown. Bottom right panel: Fine mode (FM) fraction associated to the CISAR aerosol retrieval.

Despite not exploiting any external cloud mask, CISAR is also capable of correctly retrieving the position of both thick and thin clouds close to the African Western coast, visible in the red colour scale in Figure 8, where only COT retrievals higher than 2 are shown to better observe the AOT retrieval. However, CISAR retrieves a low cloud optical thickness (COT<2.) within a few kilometres away from the clouds. [46] showed that cloud contamination can be observed within 15 km away from the clouds; with its ability to retrieve both AOT and COT within the same pixels, CISAR not only improves the aerosol product spatial coverage but also addresses the issue of cloud contamination from nearby clouds without the need of a safety zone. On the other hand, CISAR's tendency to retrieve a small COT also a few kilometres away from clouds could result in a slight underestimation of the AOT, due to a not optimal aerosol/cloud discrimination.

Video S1 in the supplementary material shows the temporal evolution of the Godzilla dust storm as observed by the CISAR algorithm, together with the false colour composite from SLSTR bands S1, S2 and S3. During the time series, it can be seen that CISAR correctly follow the spatial and temporal variability of the dust storm originating close to the African coast around the 14th of June 2020 and being transported over the Atlantic ocean. Godzilla reaches the Caribbean islands on the 21st of June, with a CISAR retrieved AOT of about 1. During the time series in Video S1 in the supplementary material, it can be seen how CISAR correctly retrieves the position of clouds, solely relying on the SLSTR observations and the prior information built from the TOA BRF spectral signature with respect to the clouds one, without any external cloud masking operation. It is also possible to visually observe the effect of the sensor dual view on CISAR retrieval. As seen in Section 2.3.1,

Preprints (www.preprints.org) | NOT PEER-REVIEWED | Posted: 31 March 2022 doi:10.20944/preprints202203.0406.v1

most of the information content is carried by the oblique view, leading to differences in the CISAR retrieval when only observations acquired in the nadir view are available. This leads to sharp discontinuities in the CISAR product, such as during the 20th of June over the Atlantic ocean.

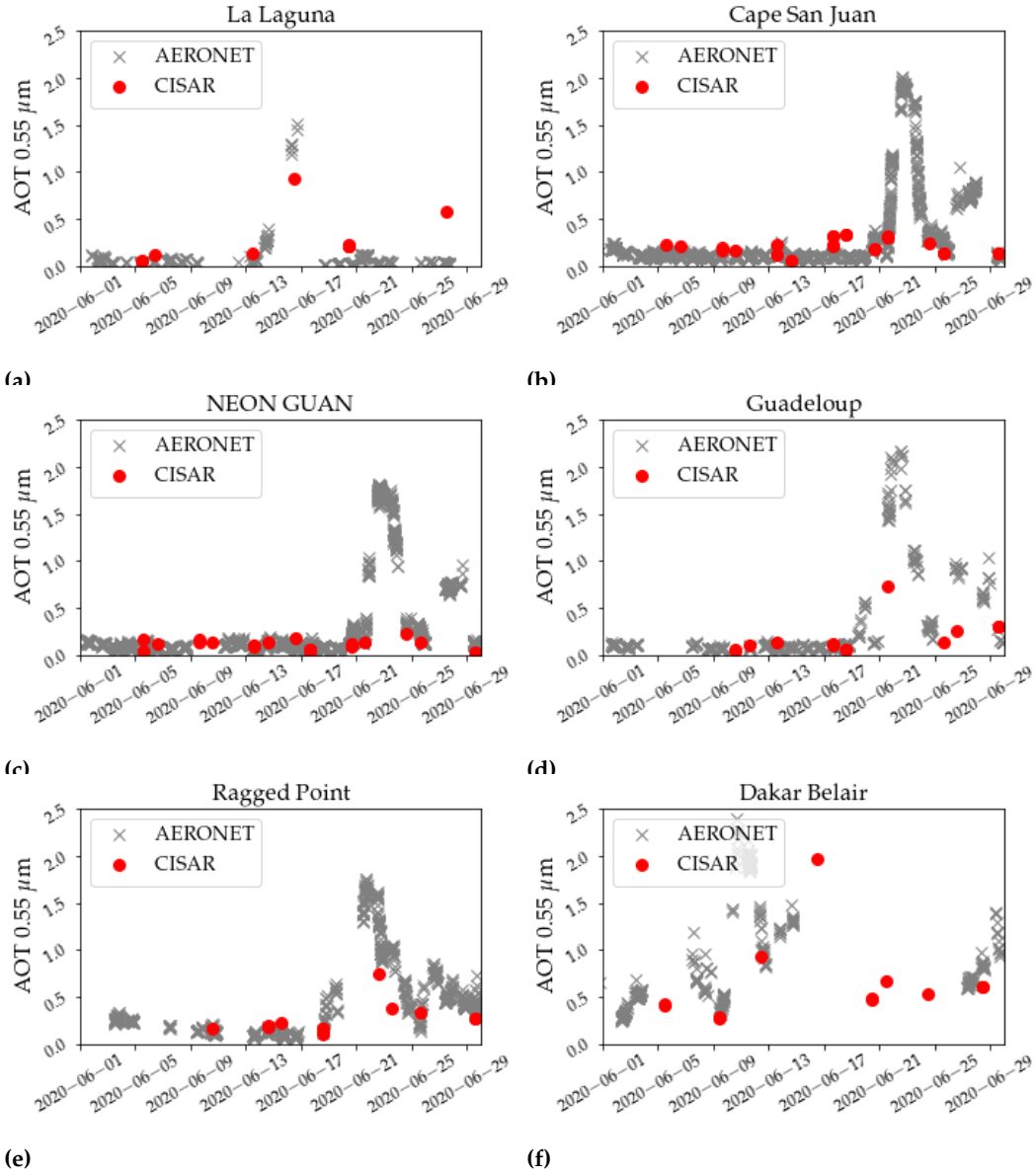

Figure 9. AOT timeseries over 6 AERONET stations affected by the Godzilla dust storm.

Figure 9 evaluates the retrieval of the AOT at 0.55 µm against AERONET observations. It can be seen that CISAR retrieves correctly the temporal evolution of the aerosol load during June 2020, although unfortunately, no SLSTR observations were available over Cape San Juan and NEON GUAN when Godzilla reached these stations. It should also be stressed here that in this exercise point measurements from the AERONET stations are being compared with satellite retrievals at 10 km. It is therefore expected to observe some discrepancies between the two datasets, as the dust storm moves quickly and its thickness can vary within a few kilometres [47]. Despite some underestimation which could be partially explained by the different spatial resolutions, CISAR correctly retrieves the increase in the aerosol load both close to the African coast (La Laguna, Dakar) and the Caribbean islands (Ragged Point, Guadeloupe). At the same time, CISAR correctly retrieves low values of AOT during the days not affected by the Godzilla storm, in good agreement with AERONET. Figure 10 shows the scatterplot between the AOT at 0.55 µm as

Preprints (www.preprints.org) | NOT PEER-REVIEWED | Posted: 31 March 2022 doi:10.20944/preprints202203.0406.v1

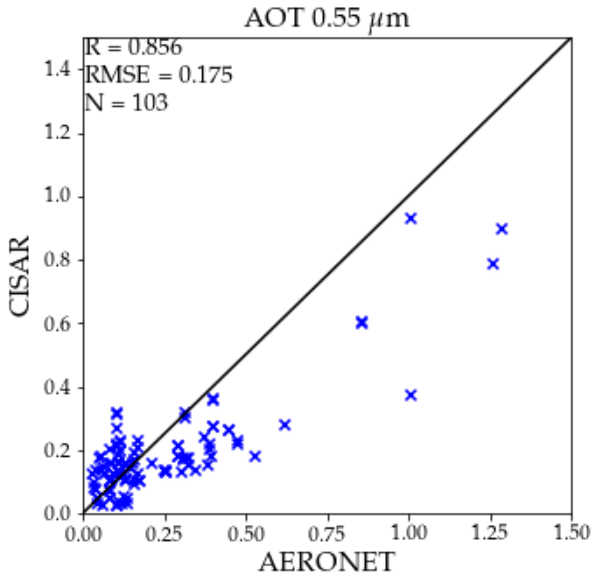

Figure 10. Scatterplot between the AOT at 0.55 µm retrieved by CISAR (y axis) and delivered by the AERONET V3 L2 product (x axis). Correlation (R), root mean square error (RMSE) and number of CISAR-AERONET collocations within a ±30 minute window (N) are shown in the plot.

delivered by CISAR and the AERONET dataset over the 6 stations listed in Figure 9. Only CISAR retrieval showing a quality indicator (QI) larger than 0 are shown in Figure 10 [19]. The resulting correlation between CISAR and AERONET is as high as 0.856.

Finally, CISAR AOT retrieval has been compared with the MODIS/Terra aerosol product MOD04 L2 v6.1[48]. Terra overpassing local time is 10:30 AM, while S3/SLSTR acquires observations at 10 AM local time. Both AOT products retrieve very high AOT (larger than 2.) at the Western African coast, although different spatial features can be observed (Figure 11). CISAR correctly retrieves the shape of the tick dust plume, also partially visible in Figure 8 (top left panel), but around it, CISAR also retrieves low values of COT. This leads to sharp borders of the dust plume and lower retrieved AOT values than in the MODIS product. Results in Figure 11 show that although CISAR can correctly retrieve high aerosol load spatial and temporal evolution, the discrimination between aerosol and thin cloud could further improve. CISAR retrieval shows slightly higher spatial coverage (especially closer to South America) as the retrieval is extended near clouds as well as within thin clouds; because of the extended spatial coverage, it is possible to observe the changes in AOT near clouds, as discussed in Section 1 [13].

4. Discussion

This paper describes an innovative approach to aerosol retrieval, where surface reflectance, aerosol and cloud single scattering properties are retrieved consistently with the same RTM, without relying on any external cloud mask. The goal of this approach is to get rid of an external cloud mask, given the strong dependency of aerosol retrieval to the masking algorithm and the number of issues linked to lost pixels and cloud contamination ([9], [4], [3], [5]).

The new version of the CISAR algorithm has been applied to S3A/SLSTR observations during June 2020 over the Atlantic ocean, when an exceptionally large dust storm event originating from the Sahara region was transported by thousand of kilometres towards the Caribbean islands. This extreme dust plume, renamed Godzilla, was mostly misclassified as cloud by the SLSTR summary cloud mask. On the 15th of June, algorithms only inverting cloud-free observations would have performed the retrieval only over 15% of all available

Preprints (www.preprints.org) | NOT PEER-REVIEWED | Posted: 31 March 2022 doi:10.20944/preprints202203.0406.v1

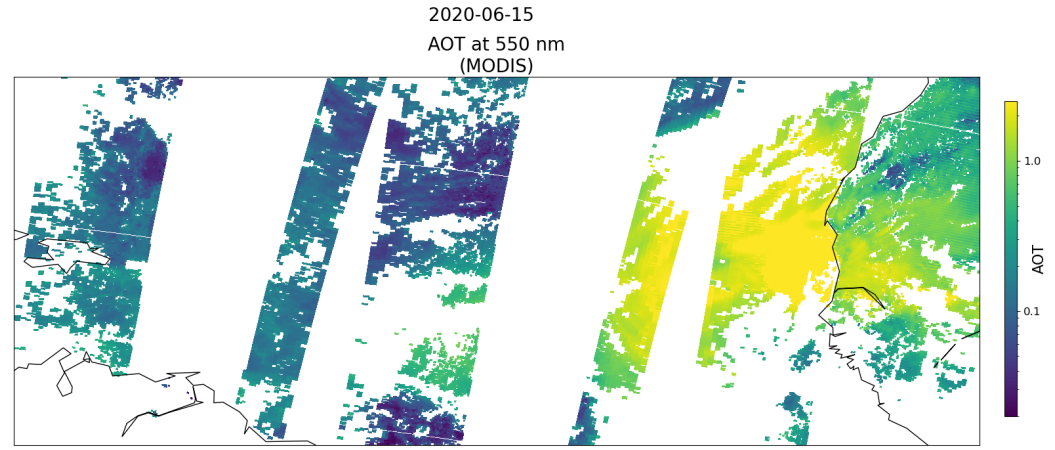

(a)

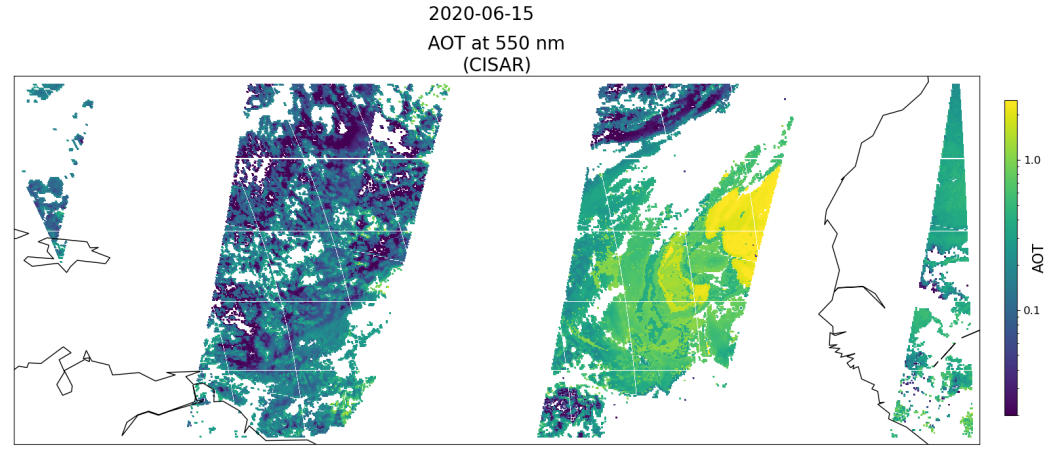

(b)

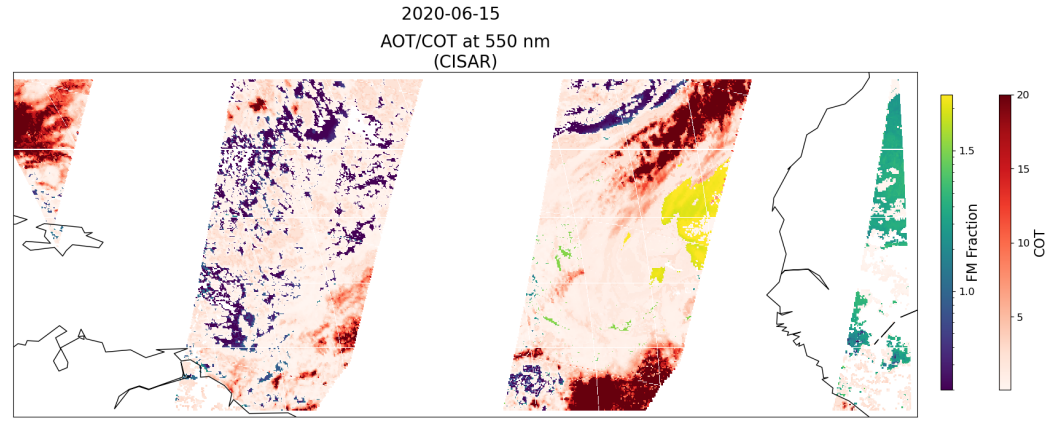

(c)

Figure 11. AOT at 0.55 µm as retrieved by the combined Dark Target and Deep blue algorithms applied to MODIS/Terra (top panel) and by CISAR (middle panel). The bottom panels show CISAR combined AOT/COT product for all COT retrieval larger than 0.1.

 doi:10.20944/preprints202203.0406.v1

SLSTR observations. CISAR AOT retrieval, however, is valid (AOT larger than 0) over more than 35% of the total number of pixels, improving the spatial coverage by a factor 2.3.

When evaluated against the AERONET dataset, the AOT retrieved by CISAR shows good agreement both in terms of magnitude and temporal evolution, with a correlation higher than 0.8 (see Figure 10). CISAR proves capable to retrieve both very low AOT in Figure 9, away from the Godzilla dust storm as well as values larger than 1.0 when the pixel is affected by the dust. Comparison against the MOD04 v6.1 MODIS product in Figure 11 shows that although CISAR correctly identified the high aerosol load, it tends to underestimate it with respect to MODIS as a low value of COT (lower than 2) is also retrieved within the same pixel by the CISAR algorithm. This results in the total optical thickness being in good agreement with the MODIS product but differently distributed between the aerosols and clouds. Compared to the MODIS MOD04 v6.1, the CISAR retrievals extend to near clouds, where it can be seen the increased AOT due to the aerosol particle swelling caused by more hydration. Also, the Godzilla dust storm is correctly identified as coarse mode by the CISAR algorithm, although the fine-coarse mode discrimination degrades as the AOT decreases, as shown in Video S2 in the supplementary material of the fine mode fraction during the second half of June 2020, available in the supplemental materials. Overall, the evaluation of the CISAR aerosol retrieval against AERONET and MODIS products shows encouraging results. Furthermore, despite the main focus of the retrieval remaining the aerosol single scattering properties, CISAR is capable of correctly identifying clouds without relying on any external pre-processing algorithm. The magnitude of the retrieved COT is also consistent with the false colour composite obtained from SLSTR observations. The cloud product retrieved by CISAR could be more extensively studied and validated in future work.

Results in Section 3 confirm the possibility of approaching aerosol retrieval in an innovative way, overcoming the need for an external cloud mask with all the issues associated with it (lost pixels, cloud contamination, etc.). The uniqueness of such a continuous product between clouds and aerosols represents a powerful tool for better studying and understanding the aerosol properties in the vicinity of clouds. Several recent studies suggest that performing the retrieval of aerosol particles only in clear-sky conditions could lead to a significant negative underestimation in the aerosol direct radiative effect [17]. The CISAR product, extending the aerosol retrieval in the vicinity and within thin clouds, could be exploited to study more extensively aerosol properties far from clear-sky conditions, as suggested by [15] and [16].

The proposed approach still has some limitations. The quality of the CISAR retrieval depends on the information content associated with the satellite observations; in the case of SLSTR, this is visible in the sharp edges in the AOT product at the overlap between the oblique and nadir view (Section 3), where the amount of information is strongly reduced due to the observation geometry, as seen in Section 2.3.1. Also, the discrimination between aerosols and thin clouds is not always successful, as discussed in Section 3. The current implementation of the spectral constraints on the surface reflectance excludes snow pixels from the retrieval. A continuous effort is made to address these limitations and further improve the CISAR algorithm. Finally, being based on the inversion of a 1D radiative transfer model, any 3D effects between clouds and clear-sky pixels cannot be correctly characterised with the CISAR algorithm.

The proposed, ambitious, method paves the way for an innovative and critical approach to aerosol retrieval, aiming at deepening the knowledge of aerosols in the vicinity of clouds by delivering a continuous aerosol-cloud product. To achieve such an ambitious objective the CISAR algorithm solution space has been extended to clouds. By being able to retrieve both aerosol and cloud single scattering properties CISAR is no longer dependent on a pre-processing cloud identification. By appropriate choice of the prior information and associated uncertainty on all the state variables, CISAR can retrieve the state of the observed system through the optimal estimation (OE) approach. With such an innovative product not only the spatial coverage of the aerosol product is improved, but it is also

possible to analyse the effect of aerosol swelling near clouds and the cloud-induced changes in their optical properties [14].

Author Contributions: Conceptualization, M.L.; Observation: M.L.; Methodology, Y.G. and M.L; Writing—original draft, M.L.; Writing—review and editing, Y.G; Software, M.L. and L.F. All authors have read and agreed to the published version of the manuscript.

Data Availability Statement: Data can be made available on request.

Supplementary Materials: The following supporting information can be downloaded at the website of this paper posted on Preprints.org. Video S1: Time series of the false colour composite from SLSTR bands S1, S2 and S3 and combined AOT/COT retrieval over the Atlantic Ocean during the Godzilla dust storm in June 2020. Video S2: Time series of the false colour composite from SLSTR bands S1, S2 and S3 and Fine Mode Fraction retrieval over the Atlantic Ocean during the Godzilla dust storm in June 2020.

Acknowledgments: This work has been performed in the framework of ESA/SEOM project CIRCAS and ESA projects aerosol_cci+ under the contracts 4000121362/17/I-NB and AO/1-9322/18/I-NB respectively.

Conflicts of Interest: The authors declare no conflict of interest.

References

1. Stocker, T.; Qin, D.; Plattner, G.K.; Tignor, M.; Allen, S.; Boschung, J.; Nauels, A.; Xia, Y.; Bex, V.; Midgley, P. Climate Change 2013: The Physical Science Basis. Contribution of Working Group I to the Fifth Assessment Report of the Intergovernmental Panel on Climate Change, 2013.
2. WHO. Ambient (outdoor) air pollution, 2021.
3. Holzer-Popp, T.; de Leeuw, G.; Griesfeller, J.; Martynenko, D.; Klüser, L.; Bevan, S.; Davies, W.; Ducos, F.; Deuzé, J.L.; Graigner, R.G.; et al. Aerosol retrieval experiments in the ESA Aerosol_cci project. *Atmospheric Measurement Techniques* **2013**, *6*, 1919–1957. doi:10.5194/amt-6-1919-2013.
4. Remer, L.A.; Mattoo, S.; Levy, R.C.; Heidinger, A.; Pierce, R.B.; Chin, M. Retrieving aerosol in a cloudy environment: aerosol product availability as a function of spatial resolution. *Atmospheric Measurement Techniques* **2012**, *5*, 1823–1840. doi:https://doi.org/10.5194/amt-5-1823-2012.
5. Koren, I.; Remer, L.A.; Kaufman, Y.J.; Rudich, Y.; Martins, J.V. On the twilight zone between clouds and aerosols. *Geophysical Research Letters* **2007**, *34*. doi:10.1029/2007GL029253.
6. Marshak, A.; Wen, G.; Coakley Jr., J.A.; Remer, L.A.; Loeb, N.G.; Cahalan, R.F. A simple model for the cloud adjacency effect and the apparent bluing of aerosols near clouds. *Journal of Geophysical Research: Atmospheres* **2008**, *113*. doi:https://doi.org/10.1029/2007JD009196.
7. Várnai, T.; Marshak, A. MODIS observations of enhanced clear sky reflectance near clouds. *Geophysical Research Letters* **2009**, *36*. doi:https://doi.org/10.1029/2008GL037089.
8. Chand, D.; Wood, R.; Ghan, S.J.; Wang, M.; Ovchinnikov, M.; Rasch, P.J.; Miller, S.; Schichtel, B.; Moore, T. Aerosol optical depth increase in partly cloudy conditions. *Journal of Geophysical Research: Atmospheres* **2012**, *117*. doi:https://doi.org/10.1029/2012JD017894.
9. Schwarz, K.; Cermak, J.; Fuchs, J.; Andersen, H. Mapping the Twilight Zone—What We Are Missing between Clouds and Aerosols. *Remote Sensing* **2017**, *9*, 577. doi:10.3390/rs9060577.
10. Kassianov, E.I.; Ovtchinnikov, M. On reflectance ratios and aerosol optical depth retrieval in the presence of cumulus clouds. *Geophysical Research Letters* **2008**, *35*. doi:10.1029/2008GL033231.
11. Marshak, A.; Wen, G.; Coakley, J.A.; Remer, L.A.; Loeb, N.G.; Cahalan, R.F. A simple model for the cloud adjacency effect and the apparent bluing of aerosols near clouds. *Journal of Geophysical Research: Atmospheres* **2008**, *113*. doi:10.1029/2007JD009196.
12. Poulsen, C.A.; Siddans, R.; Thomas, G.E.; Sayer, A.M.; Grainger, R.G.; Campmany, E.; Dean, S.M.; Arnold, C.; Watts, P.D. Cloud retrievals from satellite data using optimal estimation: evaluation and application to ATSR. *Atmospheric Measurement Techniques* **2012**, *5*, 1889–1910. doi:10.5194/amt-5-1889-2012.
13. Quaas, J.; Stevens, B.; Stier, P.; Lohmann, U. Interpreting the cloud cover – aerosol optical depth relationship found in satellite data using a general circulation model. *Atmospheric Chemistry and Physics* **2010**, *10*, 6129–6135. doi:10.5194/acp-10-6129-2010.
14. Spencer, R.S.; Levy, R.C.; Remer, L.A.; Mattoo, S.; Arnold, G.T.; Hlavka, D.L.; Meyer, K.G.; Marshak, A.; Wilcox, E.M.; Platnick, S.E. Exploring Aerosols Near Clouds With High-Spatial-Resolution Aircraft Remote Sensing During SEAC4RS. *Journal of Geophysical Research: Atmo-*

spheres **2019**, *124*, 2148–2173. _eprint: https://onlinelibrary.wiley.com/doi/pdf/10.1029/2018JD028989, doi:10.1029/2018JD028989.

15. Rosenfeld, D.; Sherwood, S.; Wood, R.; Donner, L. Climate Effects of Aerosol-Cloud Interactions. *Science* **2014**, *343*, 379–380, [https://www.science.org/doi/pdf/10.1126/science.1247490]. doi:10.1126/science.1247490.
16. Seinfeld, J.H.; Bretherton, C.; Carslaw, K.S.; Coe, H.; DeMott, P.J.; Dunlea, E.J.; Feingold, G.; Ghan, S.; Guenther, A.B.; Kahn, R.; et al. Improving our fundamental understanding of the role of aerosol-cloud interactions in the climate system. *Proceedings of the National Academy of Sciences* **2016**, *113*, 5781–5790. Publisher: National Academy of Sciences _eprint: https://www.pnas.org/content/113/21/5781.full.pdf, doi:10.1073/pnas.1514043113.
17. Marshak, A.; Ackerman, A.; Da Silva, A.; Eck, T.; Holben, B.; Kahn, R.; Kleidman, R.; Knobelspiesse, K.; Levy, R.; Lyapustin, A.; et al. Aerosol properties in cloudy environments from remote sensing observations: A review of the current state of knowledge. Manuscript accepted for publication, doi:10.1175/BAMS-D-20-0225.1.
18. Govaerts, Y.; Luffarelli, M. Joint retrieval of surface reflectance and aerosol properties with continuous variation of the state variables in the solution space – Part 1: theoretical concept. *Atmospheric Measurement Techniques* **2018**, *11*, 6589–6603. doi:10.5194/amt-11-6589-2018.
19. Luffarelli, M.; Govaerts, Y. Joint retrieval of surface reflectance and aerosol properties with continuous variation of the state variables in the solution space – Part 2: application to geostationary and polar-orbiting satellite observations. *Atmospheric Measurement Techniques* **2019**, *12*, 791–809. doi:10.5194/amt-12-791-2019.
20. Smith, D.L. Lessons learned from (A)ATSR and prelaunch calibration of SLSTR. Technical report, RAL Space, 2013.
21. de Leeuw, G.; Holzer-Popp, T.; Bevan, S.; Davies, W.H.; Descloitres, J.; Grainger, R.G.; Griesfeller, J.; Heckel, A.; Kinne, S.; Klüser, L.; et al. Evaluation of seven European aerosol optical depth retrieval algorithms for climate analysis. *Remote Sensing of Environment* **2015**, *162*, 295–315. doi:10.1016/j.rse.2013.04.023.
22. Jethva, H.; Torres, O.; Yoshida, Y. Accuracy assessment of MODIS land aerosol optical thickness algorithms using AERONET measurements over North America. *Atmospheric Measurement Techniques* **2019**, *12*, 4291–4307. doi:10.5194/amt-12-4291-2019.
23. Govaerts, Y. RTMOM V0B.10 User's Manual. Technical report, EUMETSAT, 2006a.
24. Govaerts, Y. RTMOM V0B.10 Evaluation report. Technical report, EUMETSAT, 2006b.
25. Dong, C. Remote sensing, hydrological modeling and in situ observations in snow cover research: A review. *Journal of Hydrology* **2018**, *561*. doi:10.1016/j.jhydrol.2018.04.027.
26. Lyapustin, A., Y.W. Mcd19a3 modis/terra+aqua brdf model parameters 8-day l3 global 1km sin grid v006. Technical report, LP DAAC, 2018b.
27. Rahman, H.; Pinty, B.; Verstraete, M.M. Coupled surface-atmosphere reflectance (CSAR) model. 2. Semiempirical surface model usable with NOAA Advanced Very High Resolution Radiometer Data. *Journal of Geophysical Research* **1993**, *98*, 20,791–20,801.
28. Lucht, W.; Schaaf, C.; Strahler, A. An algorithm for the retrieval of albedo from space using semiempirical BRDF models. *IEEE Transactions on Geoscience and Remote Sensing* **2000**, *38*, 977–998. doi:10.1109/36.841980.
29. Hall, D.K.; Riggs, G.A. Normalized-Difference Snow Index (NDSI). In *Encyclopedia of Snow, Ice and Glaciers*; Singh, V.P.; Singh, P.; Haritashya, U.K., Eds.; Springer Netherlands, 2011; pp. 779–780. doi:10.1007/978-90-481-2642-2_376.
30. Luffarelli, M.; Govaerts, Y.; Damman, A. *ASSESSING HOURLY AEROSOL PROPERTY RETRIEVAL FROM MSG/SEVIRI OBSERVATIONS IN THE FRAMEWORK OF AEROSOL_CCI2*; ESA, 2016.
31. EUMETSAT. Copernicus Sentinel-3 NRT Aerosol Optical Depth | EUMETSAT Website, 2020.
32. Andrews, E.; Sheridan, P.J.; Fiebig, M.; McComiskey, A.; Ogren, J.A.; Arnott, P.; Covert, D.; Elleman, R.; Gasparini, R.; Collins, D.; et al. Comparison of methods for deriving aerosol asymmetry parameter. *Journal of Geophysical Research: Atmospheres* **2006**, *111*. _eprint: https://onlinelibrary.wiley.com/doi/pdf/10.1029/2004JD005734, doi:10.1029/2004JD005734.
33. Hsu, N.; Tsay, S.C.; King, M.; Herman, J. Aerosol properties over bright-reflecting source regions. *IEEE Transactions on Geoscience and Remote Sensing* **2004**, *42*, 557–569. doi:10.1109/TGRS.2004.824067.
34. Wang, M.; Shi, W. Cloud Masking for Ocean Color Data Processing in the Coastal Regions. *IEEE Transactions on Geoscience and Remote Sensing* **2006**, *44*, 3196–3105. doi:10.1109/TGRS.2006.876293.

35. Liu, J.; Chen, B.; Huang, J. Discrimination and validation of clouds and dust aerosol layers over the Sahara Desert with combined CALIOP and IIR measurements. *Journal of Meteorological Research* **2014**, *28*, 185–198. doi:10.1007/s13351-014-3051-5.
36. Zhou, Y.; Levy, R.C.; Remer, L.A.; Mattoo, S.; Shi, Y.; Wang, C. Dust Aerosol Retrieval Over the Oceans With the MODIS/VIIRS Dark-Target Algorithm: 1. Dust Detection. *Earth and Space Science* **2020**, *7*, e2020EA001221. _eprint: https://onlinelibrary.wiley.com/doi/pdf/10.1029/2020EA001221, doi:10.1029/2020EA001221.
37. Monks, P.S.; Granier, C.; Fuzzi, S.; Stohl, A.; Williams, M.L.; Akimoto, H.; Amann, M.; Baklanov, A.; Baltensperger, U.; Bey, I.; et al. Atmospheric composition change – global and regional air quality. *Atmospheric Environment* **2009**, *43*, 5268–5350. doi:10.1016/j.atmosenv.2009.08.021.
38. Weinzierl, B.; Ansmann, A.; Prospero, J.M.; Althausen, D.; Benker, N.; Chouza, F.; Dollner, M.; Farrell, D.; Fomba, W.K.; Freudenthaler, V.; et al. The Saharan Aerosol Long-Range Transport and Aerosol–Cloud-Interaction Experiment: Overview and Selected Highlights. *Bulletin of the American Meteorological Society* **2017**, *98*, 1427–1451. Publisher: American Meteorological Society Section: Bulletin of the American Meteorological Society, doi:10.1175/BAMS-D-15-00142.1.
39. Engelstaedter, S.; Tegen, I.; Washington, R. North African dust emissions and transport. *Earth-Science Reviews* **2006**, *79*, 73–100.
40. Liu, J.; Chen, B.; Huang, J. Discrimination and validation of clouds and dust aerosol layers over the Sahara desert with combined CALIOP and IIR measurements. *Journal of Meteorological Research* **2014**, *28*, 185–198. doi:10.1007/s13351-014-3051-5.
41. Petit, R.H. Transport of Saharan dust over the Caribbean Islands: Study of an event. *Journal of Geophysical Research* **2005**, *110*, D18S09. doi:10.1029/2004JD004748.
42. Cornwall, W. 'Godzilla' dust storm traced to shaky northern jet stream. *Science* **2020**.
43. Huang, J.; Zhang, C.; Prospero, J.M. African dust outbreaks: A satellite perspective of temporal and spatial variability over the tropical Atlantic Ocean. *Journal of Geophysical Research: Atmospheres* **2010**, *115*, [https://agupubs.onlinelibrary.wiley.com/doi/pdf/10.1029/2009JD012516]. doi:https://doi.org/10.1029/2009JD012516.
44. Errera, Q.; Bennouna, Y.; Schulz, M.; Eskes, H.; Basart, S.; Benedictow, A.; Blechschmidt, A.M.; Chabrillat, S.; Clark, H.; Cuevas, E.; et al. Validation report of the CAMS global Reanalysis of aerosols and reactive gases, years 2003-2020 **2021**. Publisher: Copernicus Atmosphere Monitoring Service, doi:10.24380/8GF9-K005.
45. Eck, T.F.; Holben, B.N.; Reid, J.S.; Arola, A.; Ferrare, R.A.; Hostetler, C.A.; Crumeyrolle, S.N.; Berkoff, T.A.; Welton, E.J.; Lolli, S.; et al. Observations of rapid aerosol optical depth enhancements in the vicinity of polluted cumulus clouds. *Atmospheric Chemistry and Physics* **2014**, *14*, 11633–11656. doi:10.5194/acp-14-11633-2014.
46. Christensen, M.W.; Neubauer, D.; Poulsen, C.A.; Thomas, G.E.; McGarragh, R.; Povey, A.C.; Proud, S.R.; Grainger, R.G. Unveiling aerosol-cloud interactions Part 1: Cloud contamination in satellite products enhances the aerosol indirect forcing estimate **2017**. p. 24.
47. Jiang, X.; Liu, Y.; Yu, B.; Jiang, M. Comparison of MISR aerosol optical thickness with AERONET measurements in Beijing metropolitan area. *Remote Sensing of Environment* **2007**, *107*, 45 – 53. Multi-angle Imaging SpectroRadiometer (MISR) Special Issue, doi:10.1016/j.rse.2006.06.022.
48. Levy, R.; Hsu, C.; et al.. MODIS Atmosphere L2 Aerosol Product. NASA MODIS Adaptive Processing System, Goddard Space Flight Center, USA, 2015. doi:http://dx.doi.org/10.5067/MODIS/MOD0